

The impact of optimal respiratory gating and image noise on evaluation of intra-tumor heterogeneity in ¹⁸Fluorodeoxyglucose positron emission tomography imaging of lung cancer

Willem Grootjans^{1,2}, Florent Tixier^{1,3}, Charlotte S. van der Vos^{1,4}, Dennis Vriens², Catherine C. Le Rest³,
Johan Bussink⁵, Wim J.G. Oyen^{1,6}, Lioe-Fee de Geus-Oei^{1,2,4}, Dimitris Visvikis⁷, Eric P. Visser¹

¹Department of Radiology and Nuclear Medicine, Radboud university medical center, Nijmegen, The Netherlands

²Department of Radiology, Leiden University Medical Center, Leiden, The Netherlands

³Department of Nuclear Medicine, DACTIM, University Hospital Poitiers, Poitiers, France

⁴MIRA Institute for Biomedical Technology and Technical Medicine, University of Twente, Enschede, The Netherlands

⁵Department of Radiation Oncology, Radboud university medical center, Nijmegen, The Netherlands

⁶The Institute of Cancer Research and The Royal Marsden NHS Foundation Trust, London, UK

⁷INSERM, UMR1101, LaTIM, University of Brest, Brest, France

Institution where the work was performed:

1. Department of Radiology and Nuclear Medicine, Radboud university medical center, Nijmegen, The Netherlands
2. Department of Nuclear Medicine, DACTIM, University Hospital Poitiers, Poitiers, France
3. INSERM, UMR1101, LaTIM, University of Brest, Brest, France

Correspondence:

W. Grootjans M.Sc.

Department of Radiology

Leiden University Medical Center

P.O. Box 9600, 2300 RC Leiden, The Netherlands

E-mail: W.Grootjans@lumc.nl

Running title: Quantifying lung cancer heterogeneity

Keywords: ¹⁸F-FDG PET/CT; Lung cancer; Radiomics; Respiratory gating; Total lesion glycolysis

ABSTRACT

Assessment of measurement accuracy of intra-tumor heterogeneity using texture features in positron emission tomography (PET) images is essential to characterize cancer lesions with high precision. In this study, we investigated the influence of respiratory motion and varying noise levels on quantification of texture features in patients with lung cancer.

Methods: Respiratory gating was performed on list-mode data of 60 lung cancer patients, who underwent ^{18}F -fluorodeoxyglucose (FDG) PET, using an optimal respiratory gating algorithm (ORG). The ORG images were reconstructed using a duty cycle (percentage of the total acquired PET data) of 35%. In addition to ORG images, non-gated images with varying statistical quality (using 35% and 100% of PET data) were reconstructed to investigate the effects of image noise. Several global image-derived indices and texture parameters (entropy, high intensity emphasis (HIE), zone percentage (ZP), and dissimilarity) that have been associated with patient outcome, were calculated. Clinical impact of ORG and image noise on assessment of intra-tumor heterogeneity was evaluated using Cox regression models with overall survival (OS) as outcome measure for non-small cell lung cancer patients. Threshold for statistical significance was adjusted for multiple comparisons using Bonferroni.

Results: Respiratory motion significantly affected intra-tumor heterogeneity quantification for lesions in the lower lung lobes ($p < 0.007$), with the exception of entropy ($p > 0.007$). The mean increase of entropy, dissimilarity, ZP, and HIE, for lower lobe lesions was $1.3 \pm 1.5\%$ ($p = 0.02$), $11.6 \pm 11.8\%$ ($p = 0.006$), $2.3 \pm 2.2\%$ ($p = 0.002$), and $16.8\% \pm 17.2\%$ ($p = 0.006$), respectively. No significant differences were observed for lesions located in the upper lung lobes ($p > 0.007$). Differences in the statistical quality of the PET images affected the texture parameters to a lesser extent than respiratory motion, with no statistically significant differences between the images. The median follow-up time of this patient cohort was 35 months (range 7 – 39 months). In multivariate analysis for OS, total lesion glycolysis (TLG) and HIE were the two most relevant image-derived indices considered to be independent significant co-variates for the model, regardless of the image type considered.

Conclusions: The results of this study suggest that the tested textural features are robust in the presence of respiratory motion artefacts and varying levels of image noise.

INTRODUCTION

Positron emission tomography (PET) in combination with X-ray computed tomography (CT) imaging has gradually evolved from a diagnostic tool towards a multirole imaging platform for the clinical management of patients diagnosed with lung cancer (1). The advantage of PET over other tomographic imaging modalities is the ability to characterize and quantify the biological landscape of cancerous lesions with high sensitivity, making it possible to identify areas that are linked to therapy resistance or are more aggressive (1).

In this regard, the development of image-derived indices with the objective to extract as much information from PET images as possible, is becoming increasingly important (2). Traditional image-derived indices used in PET typically rely on the quantification of lesion standardized uptake values (SUVs) and overall tumor volume, which have been shown to be independent prognostic factors for patient outcome and treatment response (3). Although useful, these parameters omit available information related to the spatial distribution and specific features regarding intra-tumor radiotracer accumulation, which may limit the possibility to further characterize the biological behavior of the tumor.

Interest in the quantification of intrinsic spatial and temporal heterogeneity in solid malignancies has been growing over the last few years. Particularly, the role of quantifying intra-tumor heterogeneity using medical imaging for identifying specific tumor phenotypes (4), prediction of treatment resistance (5-7), and overall survival (OS) (8) is increasingly being recognized. This view fits our current knowledge of cancer, in which malignant lesions consist of heterogeneous cell populations with distinct molecular and micro-environmental differences (9). Hence the current interest in using medical imaging to repetitively assess intra-tumor spatial and temporal heterogeneity (4).

However, in order to characterize cancer lesions with high precision, assessment of measurement accuracy of such indices under different imaging conditions is essential (10,11). The accuracy and robustness of these measurements is related to the PET acquisition and reconstruction protocols, as well as variability in patient physiology. In particular, motion-blurring due to respiration can significantly influence quantification of lung lesion features in PET images (12,13). Furthermore, it has been reported that PET texture features can be sensitive to variations in statistical quality and normal stochastic variations in images (14). In this study, we investigated the

clinical impact of respiratory gating and varying image noise levels on quantification of several textural features in high resolution time-of-flight PET imaging with the glucose analogue 18F-fluorodeoxyglucose (FDG).

MATERIALS AND METHODS

Patients

The institutional review board of the Radboud university medical center approved this retrospective study and the requirement to obtain informed consent was waived. A total of 60 patients of our fast-track outpatient diagnostic program with histologically proven lung cancer were included in this study. Only lesions with a minimum volume of 3 cm³ were included since this has been previously indicated as the minimum lesion size for the calculation of meaningful and of complementary information on intra-tumoral heterogeneity in FDG-PET images using textural feature analysis (15). Patient characteristics are summarized in Table 1.

Image acquisition and reconstruction

Whole body FDG-PET imaging was performed using a Biograph 40 mCT (Siemens Medical Solutions, Knoxville TN, USA) PET/CT scanner. The amount of administered FDG was adjusted to the patients' weight (3.2±0.3 MBq/kg). Full details regarding image acquisition and reconstruction have been described previously (12,16). In short, bed positions covering the thorax and upper abdomen were acquired in list-mode with a duration of 6 minutes per bed position and the respiratory signal was obtained using an AZ-733V respiratory gating system (Anzai Medical Co Ltd, Tokyo, Japan). Reconstruction was performed using 3 iterations, 21 subsets (Ultra-HD PET), and a transaxial matrix size of 400×400 voxels. Post reconstruction filtering was performed using a three-dimensional Gaussian filter kernel with a full width half maximum of 3.0 mm.

Respiratory gating

Respiratory gating was performed on the list-mode data using an amplitude-based optimal respiratory (ORG) algorithm, integrated in the Syngo 2011A MI.PET/CT software (HD-Chest, Siemens Medical Solutions, Knoxville TN, USA). The main user input for the ORG algorithm is the percentage duty cycle, which corresponds to the percentage of the total acquired data used for image reconstruction (12). The ORG images were reconstructed with a duty cycle of 35% (ORG_{35%}), which was previously found to provide the best balance between image quality and motion rejection (12). Non-gated images with an equivalent statistical quality as the ORG_{35%} images, were reconstructed using the first 126 seconds (35%) of the acquired PET data (non-gated_{35%}). Furthermore, non-gated images using the full 360 seconds (100%) of the acquired PET data (non-gated_{100%}) were reconstructed. The different reconstructed images used for image analysis are depicted in Figure 1.

For each patient, additional gated images during the maximum inspiration and expiration phases (by restricting the amplitude range to the minimum and maximum amplitude of the respiratory signal respectively) were reconstructed for calculation of lesion displacement during the respiratory cycle. These images were reconstructed with a duty cycle of 20% (ORG_{20%}) in order to reduce the impact of residual motion in the reconstructed PET images to a minimum. The displacement vector was determined by delineating the lesions on both PET images and subsequently calculating the distance between the lesion centroids, as depicted in Figure 2.

Image analysis

Textural features of the lesions were calculated on the ORG images and compared to the respective non-gated_{35%} images. The effect of image noise was investigated by comparing the non-gated_{35%} to the non-gated_{100%} images. Delineation of the lesions was performed using the fuzzy locally adaptive Bayesian segmentation algorithm, using 2 segmentation classes (17). Local heterogeneity parameters, describing intensity variations between each voxel and its immediate neighbors averaged over the entire volume, used for this study include entropy and dissimilarity. Regional heterogeneity parameters, considering the analysis at the level of groups of voxels and areas of various sizes and intensities, used for this study were high intensity emphasis (HIE) and zone percentage (ZP). The voxel intensities were quantized using 64-gray-levels, and local features were computed over 13 directions (18). All of the

parameters considered in this work have shown to be useful for predicting prognosis in patients with non-small cell lung cancer (NSCLC) (8). Furthermore, metabolic tumor volume (MTV), mean standardized uptake value (SUV_{mean}), and total lesion glycolysis (TLG) were extracted from the PET images.

Lesions were classified into three main anatomical categories; the upper lung lobes, middle and lower lung lobes, and the lung hilum/mediastinum (“central group”) (12). Given that different histological subtypes can have a different presentation considering the absolute and particular spatial distribution of FDG uptake on PET images, quantification of tumor texture was compared for different histological subtypes of lung cancer (19). In this regard, lesions were sorted into three histological subtypes; adenocarcinomas (AC), squamous cell carcinomas (SCC), small cell lung carcinomas (SCLCL).

Statistics

Statistical analysis was performed using SPSS Statistics 21 (IBM, Armonk New York, USA). Adjustment for multiple testing was performed using the Bonferroni correction (i.e. $p_{critical}=p_{\alpha}/k$, where $p_{critical}$ is the threshold for statistical significance, p_{α} is the alpha-probability (0.05) and k the number of performed tests). Statistical significance is then defined for $p < p_{critical}$. Statistical analysis for paired measurements was performed using the Wilcoxon signed rank test for paired variables, $p_{critical}=0.007$ (7 comparisons). The Kruskal Wallis H test was used for comparing different groups regarding tumor displacement (3 comparisons, $p_{critical}=0.02$) and histological groups (8 comparisons, $p_{critical}=0.006$). For the OS analysis, we used univariate and multivariate Cox regression analyses. In these analyses, only patients with NSCLC histology were included and OS was used as outcome measure, which was defined as the interval between the PET acquisition date and time of death. The closeout-date was August, 2015. Patients who were alive at the closeout-date were censored for OS at that date. The multivariate Cox regression models were obtained using semi-automated iterative forward and backward selection of image-derived features based on the likelihood ratio criterion. The hazard ratio’s (HRs) with their corresponding 95% confidence intervals (CIs) were reported. The maximum number of covariates was chosen to be four in order to maintain a sufficient number of events per covariate for reliable statistical assessment (20). In addition, Kaplan-Meier analysis was performed to determine the association of different PET-derived image indices with OS. All variables were split at their median, to

prevent data-driven dichotomization, yielding a 'low' and 'high' group of similar size. The Kaplan Meier curves were compared using the Mantel-Cox (log rank) statistics.

RESULTS

Lesion displacement

Quantification of lesion displacement for different anatomical locations showed that lesions located in the lower lobes typically exhibited the largest displacement during patient respiration which was statistically significantly different from the other anatomical groups ($p < 0.02$). The central group comprises of lesions with a more heterogeneous character, where hilar lesions typically exhibit considerable amounts of displacement while mediastinal lesions remained almost stationary. Lesions located in the upper lobe, particularly in the apical segments, showed almost no displacement. Lesion displacement as a function of anatomical location is summarized in the box and whisker plot in Figure 3.

Global image-derived indices

There was a significant increase in SUV_{mean} of $2.9 \pm 13.0\%$ ($p < 0.0001$) and decrease in MTV of $3.6 \pm 15.1\%$ ($p < 0.0001$) in the $ORG_{35\%}$ images when compared to the non-gated_{35%} PET images. However, there were no statistically significant differences in TLG as determined on the non-gated_{35%} and $ORG_{35\%}$ images ($p > 0.007$).

Texture features

Considering the entire cohort, respiratory gating did not result in statistically significant differences in the heterogeneity parameters ($p > 0.007$). The mean increase for entropy, dissimilarity, ZP and HIE between the non-gated_{35%} and $ORG_{35\%}$ images was $0.3 \pm 2.7\%$ ($p = 0.5$), $3.6 \pm 14.3\%$ ($p = 0.2$), $0.5 \pm 3.3\%$ ($p = 0.3$), $4.2 \pm 21.4\%$ ($p = 0.3$) respectively. Respiratory gating resulted in statistically significant differences of the texture parameters for lesions in the middle and lower, with exception of entropy ($p > 0.007$). The mean increase for entropy, dissimilarity, ZP and HIE, considering lesions in the lower lobes was $1.3 \pm 1.5\%$ ($p = 0.02$), $11.6 \pm 11.8\%$ ($p = 0.006$), $2.3 \pm 2.2\%$ ($p = 0.002$), and

16.8%±17.2% (p=0.006) respectively. Figure 4 depicts the different PET images of a patient with a lesion in the lower lung lobe. For the centrally located lesions, the mean increase for entropy, dissimilarity, ZP and HIE was 0.58±3.7% (p=0.6), 5.0±19.0% (p=0.4) 0.59±4.0% (p=0.9), and 4.4±27.8% (p=0.4), respectively. Lesions in the upper lobes showed a mean decrease of 0.35±1.8 (p=0.3), 1.0±7.7% (p=0.3), 0.4±2.7% (p=0.5), 1.7±13.2% (p=0.4), for entropy dissimilarity, ZP and HIE, respectively. There was no significant correlation between lesion volume and the change in heterogeneity parameters between non-gated and ORG_{35%} images.

Entropy and HIE were the features that were most affected by the change in statistical quality of the images. Comparison of the non-gated_{100%} to the non-gated_{35%} PET images showed a statistically significant difference for entropy -0.6±1.8% (p=0.002) and HIE 9.1±22.0% (p<0.0001). Dissimilarity and ZP were not significantly affected (p>0.007), with a difference of 0.7±8.0% (p=0.4), and -0.4±3.4% (p=0.2) for dissimilarity and ZP respectively. Measurement variability due to respiratory motion typically exceeded that of the variability due to differences in noise levels in the images.

Table 2 summarizes the calculated texture parameters sorted by histology group. There were no statistically significant differences between any of the texture parameters for the different histological groups (p>0.006). Furthermore, ORG did not influence characterization of intra-tumor heterogeneity for lesions with different histology with a similar data distribution on non-gated_{35%} and ORG_{35%} images.

Univariate analysis

Of the 60 patients, 53 were diagnosed with NSCLC and could be included in the OS analysis. The median follow-up time was 35 months (range 7 – 39). During this period, 38 of the 53 patients (72%) died, all due to cancer progression.

The Kaplan-Meier curves obtained for TLG were similar for all three image types, with no differences in the patients assigned to the low or high TLG groups. Figure 5 depicts the Kaplan-Meier curves for the summed TLG of all intra-pulmonary lesions larger than 3 cm³ (TLG_{all}). The OS curves of TLG_{all} dichotomized at their median were statistically significantly different with a strong association of lower TLG values with longer OS (p=0.008). Furthermore, there were only minor differences regarding the Kaplan-Meier curves obtained for entropy,

dissimilarity, ZP, and HIE between the ORG_{35%} and non-gated images. Table 3 summarizes the log rank comparison of the OS curves for several image-derived indices.

The covariates used in the univariate Cox regression analysis with their respective hazard ratios and significance levels are summarized in Table 4 and 5. Of the clinical covariates, treatment ($p < 0.0001$) and disease stage ($p = 0.02$) were the only significant predictors for patient OS. Of the image-derived indices, primary tumor MTV (MTV_{primary}) and TLG (TLG_{primary}) as well as TLG_{all} were significant predictors for patient OS. The SUV_{mean} of the primary tumor (SUV_{primary}) was not significantly associated with patient OS in any of the three image types. Furthermore, none of the four texture parameters extracted from the PET images were significantly predictive for OS in this patient group.

Multivariate analysis

Given that patient treatment and clinical stage had a statistically significant association with OS in this patient cohort and are generally known to have a strong association with OS, we forced these two covariates in the multivariate model. The multivariate models obtained through iterative likelihood backward selection of relevant covariates are summarized in Table 6. There were no differences in the multivariate models obtained by forward and backward selection of covariates for all three images types. In these models HIE and TLG_{all} were included as independent prognostic image-derived parameters.

DISCUSSION

In this study, we have shown that patient respiration during PET imaging affects quantification of intra-tumor heterogeneity of glucose metabolism, specifically for lesions located in the lower lung lobes. Furthermore, results showed that differences in the statistical quality of the PET images affected the texture parameters to a lesser extent than respiratory motion, with no statistically significant differences between the images. The blurring effect of respiratory motion on quantification of intra-tumor heterogeneity was shown in studies by Yip et al. (13), and Oliver et al. (21). Although our results are in line with these studies, the observed differences were usually small. Furthermore, the clinical impact of the observed differences was limited, with no differences in the models for OS.

With the ORG algorithm, we were able to solely evaluate the effect of respiratory motion on quantification of intra-tumor heterogeneity and to reduce the confounding effects of varying noise levels, which is more challenging with other respiratory gating methods (12). In the current study, we have shown that the blurring effect due to respiratory motion had the largest impact on lesions located in the middle and lower lung lobes, while respiratory motion had only a limited effect on lesions in the upper lung lobes. The effect of respiratory motion on blurring of centrally located lesions was more variable, where hilar lesions could demonstrate considerable blurring while central mediastinal lesions were frequently affected to a lesser extent. These results were supported by analysis of tumor motion, where lesions in the lower lung lobes demonstrated the largest displacements.

Although respiratory motion has shown to have considerable impact on quantification of lesion SUV_{mean} and MTV (12), the effect was limited in this patient population. Particularly, ORG did not significantly influence quantification of TLG. This might be due to the pre-selection of lesions for the purpose of feature extraction in which only lesions with a volume larger than 3 cm^3 were analyzed. Therefore, only few lower lung lobe lesions could be analyzed in this study. Given that the largest blurring effect due to patient respiration is on lesions located in the lower lung lobes, this asymmetrical distribution could have resulted in underestimation of the blurring effects of respiratory motion. In addition, the increase in SUV_{mean} in the ORG images might be cancelled out by the reduction in MTV, making TLG a parameter that is more robust in the presence of respiratory motion artefacts.

One of the limitations of the current study is that a relatively small patient cohort could be analyzed. This limitation, in combination with the retrospective character of this study, limits the possibility to identify which of the parameters are truly associated with OS. Identification and validation of image features that are associated with patient outcome and OS requires a multicenter prospective study setup. Although these texture parameters have been previously associated with patient OS (8), this was not the case in the current patient cohort. This could be due to the relatively large number of patients included with metastatic disease, which was an exclusion criterion in the previous study (8). In patients with metastatic disease, characteristics of the primary tumor might have limited predictive value regarding OS, while indices containing more information about disease load (such as TLG_{all}), might more accurately predict patient OS.

The obtained multivariate models for OS were consistent over all three image types, suggesting that measurement accuracy of the calculated features are robust in the presence of respiratory motion artefacts and varying noise levels. In these multivariate models, TLG and HIE were the only independent image-derived covariates that were relevant for the clinical model, even after correction for treatment and disease stage.

Although we have studied the influence of important sources of measurement variability on quantification of intra-tumor heterogeneity, several other important sources that can contribute to measurement variability are remaining. Indeed, measurement variability in PET can stem from a myriad of different factors, ranging from acquisition and reconstruction settings to patient physiology (22). There have been reports on the variability of radiomics features in FDG-PET due to test-retest variability (18,23). In a study conducted by Leijenaar and colleagues, the investigated radiomics features showed a high stability in an inter-observer and test-retest setup (23). Furthermore, Tixier et al. reported that several texture features derived from PET images showed a high degree of reproducibility as determined on double baseline PET acquisitions (18). It is essential to assess the clinical impact of such measurement variations for the development and validation of new image-derived indices to characterize cancer lesions using PET.

CONCLUSION

The results of this study suggest that the tested textural features are robust in the presence of respiratory motion artefacts and varying levels of image noise.

ACKNOWLEDGMENTS

W. Grootjans is the recipient of an educational grant from Siemens Healthcare, The Hague, The Netherlands

REFERENCES

1. Grootjans W, de Geus-Oei L-F, Troost EGC, Visser EP, Oyen WJG, Bussink J. PET in the management of locally advanced and metastatic NSCLC. *Nat Rev Clin Oncol*. 2015;12:395-407.
2. Visvikis D, Hatt M, Tixier F, Le Rest CC. The age of reason for FDG PET image-derived indices. *Eur J Nucl Med Mol Imaging*. 2012;39:1670-1672.
3. Im H-J, Pak K, Cheon G, et al. Prognostic value of volumetric parameters of 18F-FDG PET in non-small-cell lung cancer: a meta-analysis. *Eur J Nucl Med Mol Imaging*. 2015;42:241-251.
4. Parmar C, Leijenaar RTH, Grossmann P, et al. Radiomic feature clusters and prognostic signatures specific for lung and head & neck cancer. *Sci Rep*. 2015;5:1-10.
5. Cook GJR, Yip C, Siddique M, et al. Are pretreatment 18F-FDG PET tumor textural features in non-small cell lung cancer associated with response and survival after chemoradiotherapy? *J Nucl Med*. 2013;54:19-26.
6. Cook GJR, O'Brien ME, Siddique M, et al. Non-small cell lung cancer treated with erlotinib: heterogeneity of 18F-FDG Uptake at PET—association with treatment response and prognosis. *Radiology*. 2015;276:883-93.
7. Pyka T, Bundschuh RA, Andratschke N, et al. Textural features in pre-treatment [F18]-FDG-PET/CT are correlated with risk of local recurrence and disease-specific survival in early stage NSCLC patients receiving primary stereotactic radiation therapy. *Radiat Oncol*. 2015;10:1-9.
8. Tixier F, Hatt M, Valla C, et al. Visual versus quantitative assessment of intratumor 18F-FDG PET uptake heterogeneity: prognostic value in non-small cell lung cancer. *J Nucl Med*. 2014;55:1235-1241.
9. Hanahan D, Weinberg RA. Hallmarks of cancer: the next generation. *Cell*. 2011;144:646-674.
10. Fave X, Cook M, Frederick A, et al. Preliminary investigation into sources of uncertainty in quantitative imaging features. *Comput Med Imaging Graph*. 2015;44:54-61.
11. Leijenaar RTH, Nalbantov G, Carvalho S, et al. The effect of SUV discretization in quantitative FDG-PET radiomics: the need for standardized methodology in tumor texture analysis. *Sci Rep*. 2015;5:1-10.
12. Grootjans W, de Geus-Oei L-F, Meeuwis AW, et al. Amplitude-based optimal respiratory gating in positron emission tomography in patients with primary lung cancer. *Eur Radiol*. 2014;24:3242-3250.

13. Yip S, McCall K, Aristophanous M, Chen AB, Aerts HJWL, Berbeco R. Comparison of texture features derived from static and respiratory-gated PET images in non-small cell lung cancer. *PLoS One*. 2014;9:1-14.
14. Nyflot MJ, Yang F, Byrd D, Bowen SR, Sandison GA, Kinahan PE. Quantitative radiomics: impact of stochastic effects on textural feature analysis implies the need for standards. *J Med Imaging (Bellingham)*. 2015;2:1-13
15. Hatt M, Majdoub M, Vallières M, et al. 18F-FDG PET uptake characterization through texture analysis: investigating the complementary nature of heterogeneity and functional tumor volume in a multi-cancer site patient cohort. *J Nucl Med*. 2015;56:38-44.
16. Grootjans W, Hermsen R, van der Heijden EHF, et al. The impact of respiratory gated positron emission tomography on clinical staging and management of patients with lung cancer. *Lung Cancer*. 2015;90:217-223.
17. Hatt M, Le Rest CC, Turzo A, Roux C, Visvikis D. A fuzzy locally adaptive Bayesian segmentation approach for volume determination in PET. *IEEE Trans Med Imaging*. 2009;28:881-893.
18. Tixier F, Hatt M, Le Rest CC, Le Pogam A, Corcos L, Visvikis D. Reproducibility of tumor uptake heterogeneity characterization through textural feature analysis in 18F-FDG PET. *J Nucl Med*. 2012;53:693-700.
19. Schuurbiens OCJ, Meijer TWH, Kaanders JHAM, et al. Glucose metabolism in NSCLC is histology-specific and diverges the prognostic potential of 18FDG-PET for adenocarcinoma and squamous cell carcinoma. *J Thorac Oncol*. 2014;9:1485-1493.
20. Peduzzi P, Concato J, Feinstein AR, Holford TR. Importance of events per independent variable in proportional hazards regression analysis II. Accuracy and precision of regression estimates. *J Clin Epidemiol*. 1995;48:1503-1510.
21. Oliver JA, Budzevich M, Zhang GG, Dilling TJ, Latifi K, Moros EG. Variability of image features computed from conventional and respiratory-gated PET/CT images of lung cancer. *Transl Oncol*. 2015;8:524-534.
22. Boellaard R. Standards for PET Image acquisition and quantitative data analysis. *J Nucl Med*. 2009;50:115-205.
23. Leijenaar RTH, Carvalho S, Velazquez ER, et al. Stability of FDG-PET radiomics features: an integrated analysis of test-retest and inter-observer variability. *Acta Oncol*. 2013;52:1391-1397.

Figures and figure legends

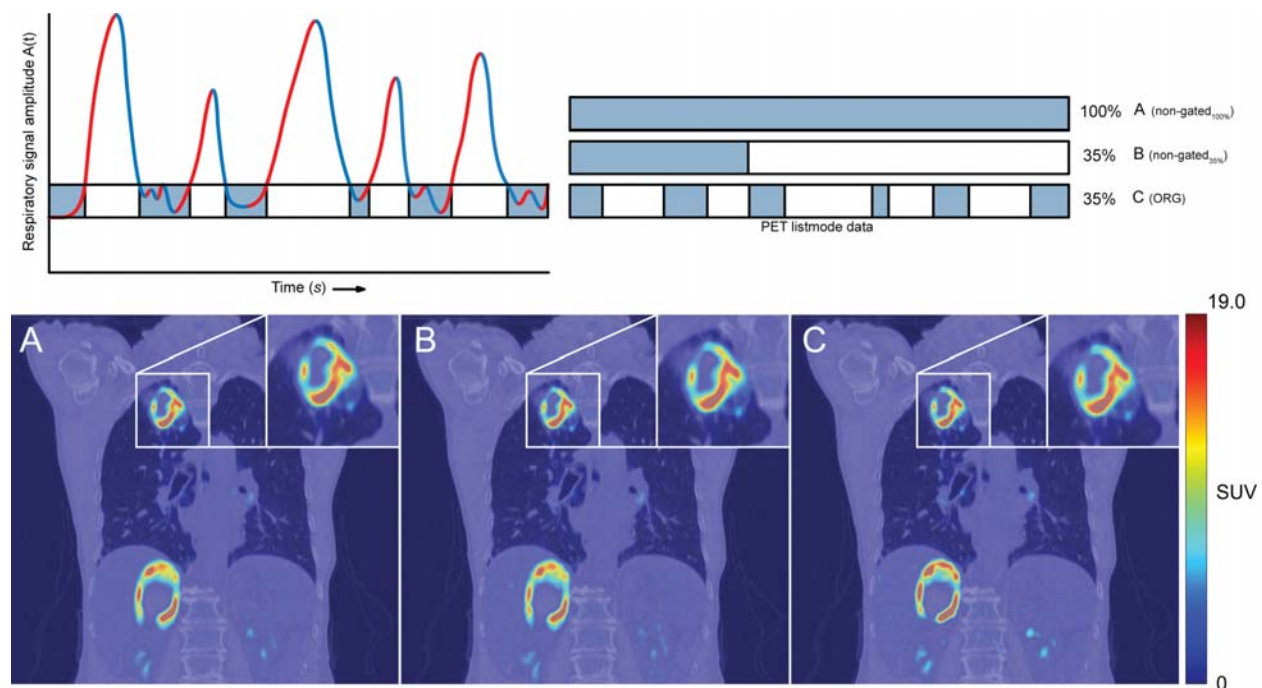


Figure 1 | Reconstructed PET images used for image analysis. ORG is performed through rebinning of list-mode data according to a respiratory signal that is simultaneously acquired. A) Non-gated_{100%} image, B) Non-gated_{35%} image, C) ORG_{35%} image.

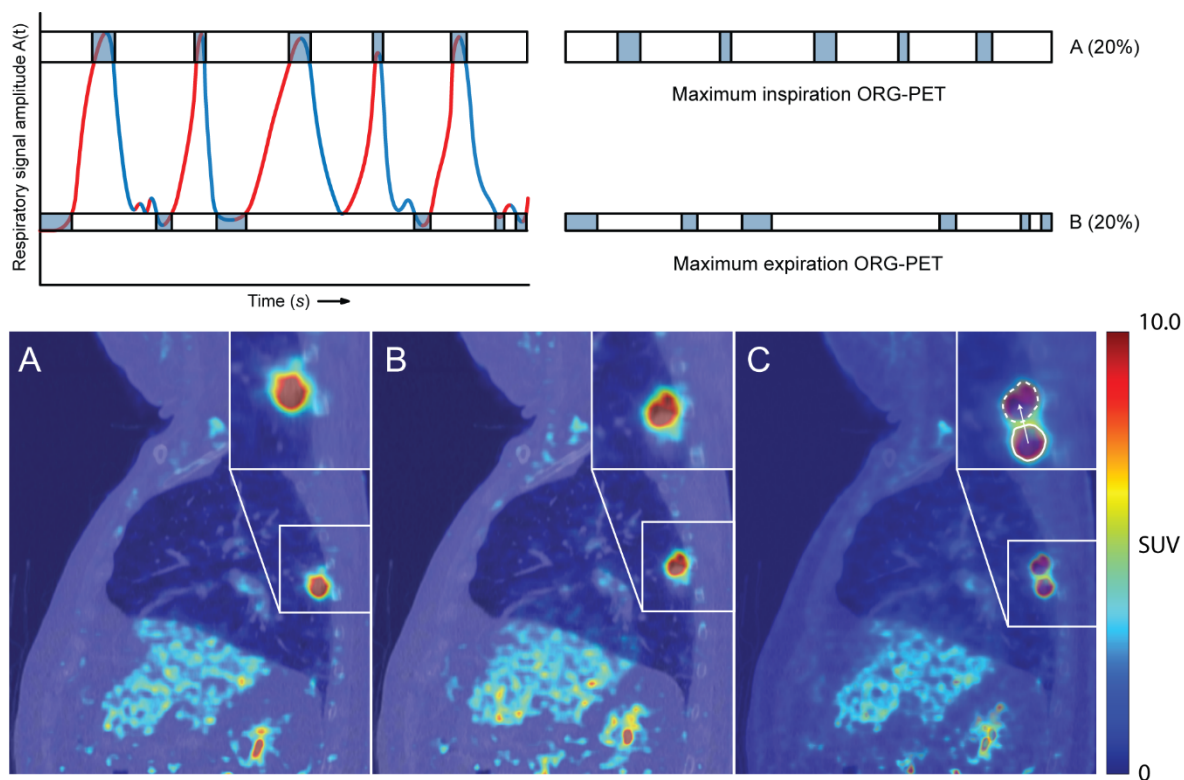


Figure 2 | Analysis of tumor displacement due to the respiratory cycle. A) Maximum inspiration ORG-PET ($ORG_{20,max}$), B) Maximum expiration ORG-PET ($ORG_{20,min}$), C) $ORG_{20,max}$ fused with $ORG_{20,min}$. The displacement vector (white arrow) is calculated by segmenting the lesion on the $ORG_{20,min}$ (dashed contour) and $ORG_{20,max}$ (solid contour) and determining the difference between the lesion's centroid on both images.

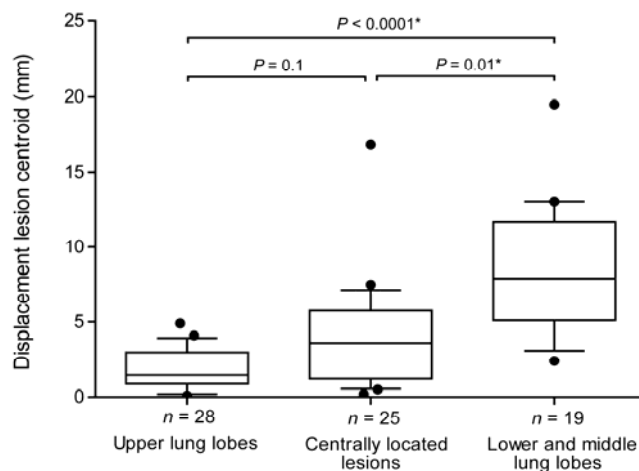


Figure 3 | Quantification of lesion displacement as a function of anatomical group. Whiskers indicate the 10 and 90 percentile, outliers are indicated by a dot. Statistical significant differences between the groups are indicated by an asterisk “*”

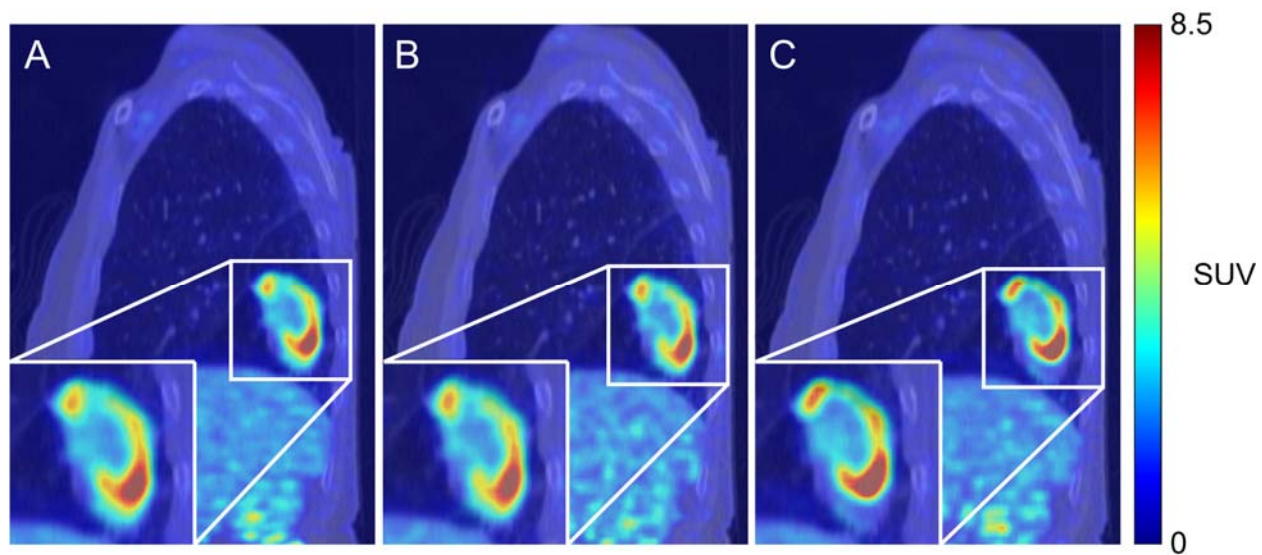


Figure 4 | ORG_{35%} and non-gated images of a patient with a NSCLC lesion in the right lower lung lobe. A) Non-gated_{100%} image, B) Non-gated_{35%} image, C) ORG_{35%} image.

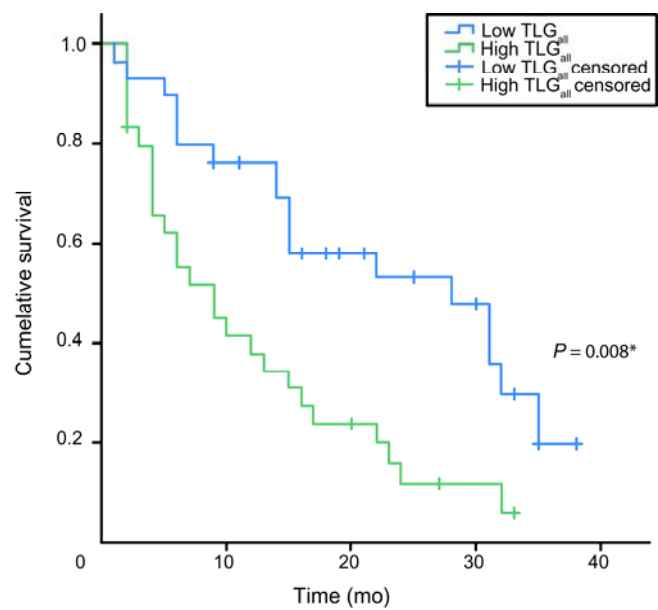


Figure 5 | Kaplan-Meier survival curves of TLG_{all}.

Tables and table legends

Table 1 | Patient characteristics

Male(Female)	43(17)
Median age (range) [y]	68(49-85)
Body mass* [kg]	77±15
Administered FDG activity* [MBq]	249±48
Incubation time FDG* [min]	79±15
Histological type	
Small cell lung cancer	7
Non-small cell lung cancer	
Squamous cell carcinoma	28
Adenocarcinoma	25
Disease stage†	
IA	5
IB	4
IIA	6
IIB	2
IIIA	17
IIIB	10
IV	16

*Data are reported as mean± standard deviation, †Disease stage according to the 7th revision of the International Association for the Study of Lung Cancer

Table 2 | Quantification of intra-tumor heterogeneity of glucose metabolism for different lung cancer histological subtypes on non-gated_{35%} and ORG_{35%} images.

Texture Parameter	Non-gated _{126s}				ORG			
	AC (n=25)	SCC (n=28)	SCLC (n=7)	Significance level	AC (n=25)	SCC (n=28)	SCLC (n=7)	Significance level
Entropy	7.29±0.28	7.70±0.31	7.21±0.26	$\chi^2=2.9$, $p=0.2$	7.31±0.29	7.35±0.29	7.24±0.28	$\chi^2=1.1$, $p=0.6$
Dissimilarity	8.62±1.76	9.00±1.92	9.11±2.57	$\chi^2=0.93$, $p=0.6$	8.92±1.85	9.12±2.07	9.57±2.42	$\chi^2=0.64$, $p=0.7$
ZP	0.85±0.04	0.86±0.05	0.85±0.05	$\chi^2=2.3$, $p=0.3$	0.86±0.05	0.86±0.05	0.87±0.05	$\chi^2=0.65$, $p=0.7$
HIE	519±182	554±156	483±128	$\chi^2=1.6$, $p=0.5$	539±195	561±157	477±134	$\chi^2=1.4$, $p=0.5$

Data are reported as mean ± standard deviation

Table 3 | Log rank comparison of Kaplan-Meier curves for different image-derived indices.

	Non-gated_{126s}	ORG	Non-gated_{360s}
MTV _{primary}	p=0.2	p=0.06	p=0.2
TLG _{primary}	p=0.03*	p=0.03*	p=0.03*
TLG _{all}	p=0.008*	p=0.008*	p=0.008*
Entropy	p=0.6	p=0.3	p=0.9
Dissimilarity	p=0.4	p=0.3	p=0.2
ZP	p=0.6	p=0.2	p=0.4
HIE	p=0.6	p=0.1	p=0.1

*=statistically significant

Table 4 | Univariate Cox regression analysis of clinical covariates for OS.

Covariate	HR	95% CI	Significance level
Treatment			p<0.0001*
Surgery	1		
Chemoradiotherapy	0.5	(0.3 – 0.9)	
Chemotherapy	1.7	(1.0 – 2.9)	
Expectative (no treatment)	3.3	(1.7 – 6.3)	
Stage			p=0.02*
I	1		
II	0.4	(0.07 – 1.9)	
III	1.6	(0.6 – 4.4)	
IV	4.3	(1.4 – 13)	
Histology			p=0.3
Adenocarcinoma	1		
Squamous cell carcinoma	0.7	(0.4 – 1.4)	
Age	1.01	(1.0 – 1.1)	p=0.4

* = statistically significant

Table 5 | Univariate analysis of patient OS of image-derived covariates. HRs are indicated per 100 units change for TLG and per 1 unit change for other the parameters.

Parameter	Non-gated _{35%}		ORG		Non-gated _{100%}	
	HR (95% CI)	Significance level	HR (95% CI)	Significance level	HR (95% CI)	Significance level
MTV _{primary}	1.009 (1.003–1.016)	p=0.004*	1.010 (1.003–1.016)	p=0.003*	1.009 (1.003–1.015)	p=0.004*
SUV _{primary}	1.00 (0.95–1.06)	p=0.9	1.00 (0.94–1.05)	p=0.8	1.00 (0.94–1.06)	p=0.9
TLG _{primary}	1.08 (1.02–1.14)	p=0.004*	1.08 (1.03–1.13)	p=0.003*	1.08 (1.03–1.14)	p=0.003*
TLG _{all}	1.09 (1.03–1.14)	p=0.002*	1.08 (1.03–1.14)	p=0.002*	1.08 (1.03–1.14)	p=0.002*
Entropy	0.3 (0.2–1.8)	p=0.3	0.4 (0.1–1.2)	p=0.1	0.7 (0.3–2.0)	p=0.5
Dissimilarity	0.9 (0.70–1.1)	p=0.2	0.9 (0.7–1.0)	p=0.09	0.9 (0.8–1.1)	p=0.2
ZP	0.01 (0–16)	p=0.2	0.002 (0–1.5)	p=0.07	0.3 (0–79)	p=0.7
HIE	0.998 (0.996–1.00)	p=0.1	0.998 (0.996–1.00)	p=0.06	0.998 (0.996–1.00)	p=0.07

*=statistically significant

Table 6 | Multivariate Cox regression models for OS. HRs are indicated per 100 units change for TLG and per 1 unit change for other the parameters.

Model	Non-gated _{35%}		ORG		Non-gated _{100%}	
	HR (95% CI)	Significance level	HR (95% CI)	Significance level	HR (95% CI)	Significance level
Fixed input						
Disease stage		0.1		0.1		0.1
I	1		1		1	
II	0.2 (0.03–1.1)		0.2 (0.03–1.1)		0.2 (0.04–1.2)	
III	1.7 (0.4–8.6)		1.4 (0.3–7.2)		1.8 (0.4–8.9)	
IV	1.8 (0.3–12)		1.7 (0.2–12)		1.9 (0.3–13)	
Treatment		<0.0001*		<0.0001*		<0.0001*
Surgery	1		1		1	
Chemoradiotherapy	0.3 (0.1–0.6)		0.3 (0.2–0.7)		0.4 (0.1–1.8)	
Chemotherapy	1.1 (0.5–2.4)		1.1 (0.5–2.5)		1.6 (0.3–8.3)	
Expectative (no treatment)	5.2 (2.2–12)		4.5 (2.0–10)		7.7 (1.5–40)	
Iterative backward selection						
TLG _{all}	1.07 (1.01–1.13)	0.02*	1.08 (1.02–1.14)	0.009*	1.07 (1.01–1.13)	0.04*
HIE	0.997 (0.995–0.999)	0.02*	0.997 (0.995–0.999)	0.02*	0.997 (0.995–0.999)	0.02*

* = statistically significant



The Journal of
NUCLEAR MEDICINE

The impact of optimal respiratory gating and image noise on evaluation of intra-tumor heterogeneity in ^{18}F -FDG positron emission tomography imaging of lung cancer

Willem Grootjans, Florent TIXIER, Charlotte S van der Vos, Dennis Vriens, Catherine C. Le Rest, Johan Bussink, Wim J. G. Oyen, Lioe-Fee de Geus-Oei, Dimitris Visvikis and Eric P. Visser

J Nucl Med.

Published online: June 9, 2016.

Doi: 10.2967/jnumed.116.173112

This article and updated information are available at:

<http://jnm.snmjournals.org/content/early/2016/06/08/jnumed.116.173112>

Information about reproducing figures, tables, or other portions of this article can be found online at:

<http://jnm.snmjournals.org/site/misc/permission.xhtml>

Information about subscriptions to JNM can be found at:

<http://jnm.snmjournals.org/site/subscriptions/online.xhtml>

JNM ahead of print articles have been peer reviewed and accepted for publication in *JNM*. They have not been copyedited, nor have they appeared in a print or online issue of the journal. Once the accepted manuscripts appear in the *JNM* ahead of print area, they will be prepared for print and online publication, which includes copyediting, typesetting, proofreading, and author review. This process may lead to differences between the accepted version of the manuscript and the final, published version.

The Journal of Nuclear Medicine is published monthly.
SNMMI | Society of Nuclear Medicine and Molecular Imaging
1850 Samuel Morse Drive, Reston, VA 20190.
(Print ISSN: 0161-5505, Online ISSN: 2159-662X)

© Copyright 2016 SNMMI; all rights reserved.

The logo for the Society of Nuclear Medicine and Molecular Imaging (SNMMI) features the letters 'S', 'N', 'M', and 'M' in a stylized, overlapping arrangement. The 'S' and 'N' are in the top row, and the 'M' and 'M' are in the bottom row. The letters are white with a red outline, set against a red square background.
SOCIETY OF
NUCLEAR MEDICINE
AND MOLECULAR IMAGING